JOURNAL OF ENVIRONMENTAL SCIENCES 102 (2021) 373–383

Available online at www.sciencedirect.com

ScienceDirect

www.elsevier.com/locate/jes

JES JOURNAL OF ENVIRONMENTAL SCIENCES

www.jesc.ac.cn

Identification of close relationship between atmospheric oxidation and ozone formation regimes in a photochemically active region

Kaihui Zhao[1], *Huihong Luo*[1], *Zibing Yuan*[1,*], *Danni Xu*[1], *Yi Du*[1], *Shu Zhang*[1], *Yuqi Hao*[1], *Yonghua Wu*[2,3], *Jianping Huang*[4,5], *Ying Wang*[6], *Rongsheng Jiang*[7]

[1] *School of Environment and Energy, South China University of Technology, Guangzhou 510006, China*
[2] *The City College of New York (CCNY), New York, NY 10031, USA*
[3] *NOAA–Cooperative Science Center for Earth System Sciences and Remote Sensing Technologies, New York, NY 10031, USA*
[4] *NOAA-NCEP Environmental Modeling Center and IM System Group Inc., College Park, MD 720740, USA*
[5] *Yale-NUIST Center on Atmospheric Environment, Nanjing University of Information Science & Technology, Nanjing 210044, China*
[6] *Xianyang Meteorological Bureau, Xianyang 712000, China*
[7] *Climate, Environment and Sustainability Center, Nanjing University of Information Science and Technology, Nanjing 210044, China*

ARTICLE INFO

Article history:
Received 5 July 2020
Revised 28 September 2020
Accepted 29 September 2020
Available online 21 October 2020

Keywords:
Atmospheric oxidation
O_3 formation regimes
WRF-CMAQ
Photochemically active region

ABSTRACT

Understanding ozone (O_3) formation regime is a prerequisite in formulating an effective O_3 pollution control strategy. Photochemical indicator is a simple and direct method in identifying O_3 formation regimes. Most used indicators are derived from observations, whereas the role of atmospheric oxidation is not in consideration, which is the core driver of O_3 formation. Thus, it may impact accuracy in signaling O_3 formation regimes. In this study, an advanced three-dimensional numerical modeling system was used to investigate the relationship between atmospheric oxidation and O_3 formation regimes during a long-lasting O_3 exceedance event in September 2017 over the Pearl River Delta (PRD) of China. We discovered a clear relationship between atmospheric oxidative capacity and O_3 formation regime. Over eastern PRD, O_3 formation was mainly in a NO_x-limited regime when HO_2/OH ratio was higher than 11, while in a VOC-limited regime when the ratio was lower than 9.5. Over central and western PRD, an HO_2/OH ratio higher than 5 and lower than 2 was indicative of NO_x-limited and VOC-limited regime, respectively. Physical contribution, including horizontal transport and vertical transport, may pose uncertainties on the indication of O_3 formation regime by HO_2/OH ratio. In comparison with other commonly used photochemical indicators, HO_2/OH ratio had the best performance in differentiating O_3 formation regimes. This study highlighted the necessities in using an atmospheric oxidative capacity-based

* Corresponding author.
E-mail: zibing@scut.edu.cn (Z. Yuan).

https://doi.org/10.1016/j.jes.2020.09.038

indicator to infer O_3 formation regime, and underscored the importance of characterizing behaviors of radicals to gain insight in atmospheric processes leading to O_3 pollution over a photochemically active region.

Introduction

Tropospheric ozone (O_3) pollution is of great concern due to its adverse effects on human health, vegetation growth, and climate change (Swackhamer, 1993; Ainsworth et al., 2012; Zhang et al., 2016; Westervelt et al., 2019). In the troposphere, O_3 is generated by a series of photochemical reactions between its precursors, volatile organic compounds (VOCs) and nitrogen oxides (NO_x, sum of nitric oxide (NO) and nitrogen dioxide (NO_2)), under conducive meteorological conditions such as high temperature, strong solar radiation, weak winds, and stable atmospheric boundary layer Logan (1989). Reduction of O_3 should be achieved by emission controls on VOCs, NO_x, or both.

However, due much to the complex chemical reactions leading to O_3 formation, O_3 responses nonlinearly to precursor changes under different O_3 formation regimes Sillman (1999). For instance, when O_3 forms in a VOC-limited regime, VOCs control decreases O_3 level while NO_x reduction would lead to O_3 increase, so-called 'NO_x disbenefits', due to the reduced titration in removing O_3. Significant increases in O_3 mixing ratio and atmospheric oxidation capacity in response to the sharp decrease of NO_x emissions in the recent Corona Virus Disease 2019 (COVID-19) outbreak over northern China provided a perfect illustration on NO_x disbenefits under a VOC-limited regime (Huang et al., 2020; Le et al., 2020; Sicard et al., 2020; Wang et al., 2020). The maximum daily 8 h average (MDA8) O_3 concentration had increased by 18% over the PRD due to the COVID-19 lockdown in China (Zhao et al., 2020).

Extensive studies have been conducted to investigate O_3-precursor nonlinearity using different methods, including photochemical indicators (e.g. Sillman et al., 1990; Sillman, 1995; Kleinman et al., 1997; Jaeglé et al., 1998), Observation-Based Model (OBM) (e.g., Cardelino and Chameides, 1995; Kumar and Russell, 1996; Cheng et al., 2010), and Emission-Based Model (EBM) (e.g., Ou et al., 2016; Sharma and Khare, 2017). Due much to its simplicity, the photochemical indicator approach has been widely applied to identify O_3 formation regimes. A series of photochemical indicators were proposed and their values quantified to separate O_3 formation regime into VOC-limited and NO_x-limited, including but not limited to, VOCs/NO_x ratio of 8 (Sillman, 1995; Sillman, 1999), H_2O_2/HNO_3 of 0.07–0.3 and O_3/NO_y of 4–6 (Sillman and He, 2002), O_3/HNO_3 of 2, O_3/NO_z of 18–22 and H_2O_2/HNO_3 of 2.5–3 Jiménez and Baldasano (2004), and H_2O_2/HNO_3 of 0.2–2.4 (Liu et al., 2010). Note that a majority of these indicators were derived from routinely monitored pollutants due to the availability of monitoring data. Although simple and direct, they cannot delineate the complex photochemical process leading to O_3 formation, posing adverse impact on the accuracy of indicating O_3 formation regime. The role of atmospheric oxidation, the core driver of O_3 formation, was largely neglected.

Atmospheric oxidation plays a critical role in O_3 and secondary fine particles production. The hydroxyl radical (OH) and hydroperoxyl radical (HO_2), called HO_x, are commonly used to characterize atmospheric oxidation. A series of studies have been performed to investigate the relationship between atmospheric oxidation and O_3 production (e.g. Monks, 2005; Mao et al., 2010; Ren et al., 2013). Previous studies have demonstrated that HO_2 oxidizing NO to produce NO_2 dominates O_3 production in late spring and summer of 2003 at Waliguan of China (Xue et al., 2013), and higher O_3 production was generally associated with greater OH production in the summer of 2006 at Houston (Mao et al., 2010). Although the impact of the atmospheric oxidation on O_3 production have been extensively studied, the impacts of atmospheric oxidation on O_3-precursor nonlinearity and O_3 formation regimes, the essential indicators for O_3 pollution control, remain a large knowledge gap.

In this study, we selected Pearl River Delta (PRD) of China as our research target area to investigate the interplay between atmospheric oxidation and O_3-precursor nonlinearity. Located in southern China, PRD is one of the most photochemically active regions in the world due to its warm weather, strong solar radiation and intense VOCs and NO_x emissions attributed to rapid urbanization and industrialization (Chan and Yao, 2008; Lu et al., 2019). PRD has been suffering from significant and worsening O_3 pollution. The annual 90th percentile of MDA8 O_3 concentration had increased by 2.1% per year since 2013 and reached 176 μg/m^3 in 2019, exceeding the national tier-II standard of 160 μg/m^3. Such a dramatic increase is largely driven by the high oxidative capacity over the region. OH and HO_2 average concentration of 0.63 pptv and 63 pptv, respectively, were measured in the summer of 2006 (Hofzumahaus et al., 2009), which are the highest OH and HO_2 levels ever recorded in the world. Such a high HO_x radical concentration poses great challenges on O_3 control, and may potentially impact O_3 formation regime. Studies showed that PRD was generally in a VOC-limited regime, but with significant diurnal and inter-episode variations (Zhang et al., 2008; Shao et al., 2009; Wang et al., 2011; Li et al., 2013; Zou et al., 2015). In general, VOCs control is the most effective way to reduce peak O_3 levels but a shift to NO_x-limited regime with stringent NO_x control is required for O_3 attainment in the long term (Ou et al., 2016). Hence, the mechanism of atmospheric oxidation, especially the role of HO_x radicals in shaping O_3 formation regimes over the PRD, deserves detailed investigation.

In this study, we applied a two-way coupled Weather Research and Forecasting – Community Multi-scale Air Quality (WRF-CMAQ) modeling system to investigate the relationship between oxidative capacity and O_3 formation regime

in September 2017, a month with long-lasting O_3 pollution episode over the PRD. Emission reduction scenario analysis was performed to identify the O_3 formation regime on each day. We demonstrated that HO_2/OH is a better indicator for O_3 formation regime in the PRD, and process analysis (PA) can explain the underlying reasons of the relationship between HO_2/OH ratio and O_3 formation regime. We thereby recommended using the HO_2/OH ratio for signaling O_3 control strategies over the PRD and other photochemically active regions worldwide alike.

1. Methodology and data

1.1. *Modeling system and configurations*

The version 5.0.2 of WRF-CMAQ modeling system was used in this study. The modeling domains were configured using the Lambert projection, with a triple-nested grid centered at 28.5°N 114°E and two true latitudes for the projection at 15°N and 40°N as the basic projected coordinate. In order to avoid interference of meteorological boundary fields during model simulation, the WRF simulation domain (**Table S1**) was slightly larger than the CMAQ simulation domain (**Table S2** and **Fig. S1a**). The outermost domain (D1) covers much of East Asia, Southeast Asia and the northwestern Pacific with a resolution of 27 km, the middle domain (D2) covers most of Guangdong province with a resolution of 9 km, and the innermost domain (D3) covers most of the PRD region with a resolution of 3 km. There are 46 vertical levels from surface to the 50-hPa level. The height of the lowest vertical layer is about 44 m above the ground level.

In WRF simulation, the Final Operational Global Analysis data (FNL) at an interval of 6 h with the horizontal resolution of 1° × 1° provided by the National Centers for Environmental Prediction (NCEP) were used for initial and boundary conditions. The land use data was retrieved from Moderate Resolution Imaging Spectroradiometer (MODIS) observation. The specific WRF parameterization scheme can be found in **Table S3**.

Anthropogenic emissions in Guangdong Province were generated based on the 2017 latest emission inventory and transformed by the SMOKE-PRD emission processor into hourly gridded model-ready emission data to be used in the WRF-CMAQ modeling system. This localized inventory included emissions from sources of power plants, fixed combustion, on-road mobile, shipping, industrial process, solvent-use, and biomass burning, for pollutants of sulfur dioxide (SO_2), carbon monoxide (CO), NO_x, anthropogenic VOCs (AVOCs), black carbon (BC), organic carbon (OC) and particulates (PM_{10} and $PM_{2.5}$). Biogenic VOCs (BVOCs) emissions were calculated by the Model of Emissions of Gases and Aerosols from Nature (MEGAN) (Guenther et al., 2012). Multi-resolution Emission Inventory for China (MEIC) Model with a 1° × 1° resolution (http://www.meicmodel.org/) and Regional Emission inventory in Asia (REAS) with a 0.25° resolution were adopted for areas in D1 and D2 outside Guangdong (Zhang et al., 2009; Kurokawa et al., 2013).

In CMAQ simulation, CB-05 gas-phase chemical mechanism and AE5 aerosol mechanism were used. Also incorporated in the CMAQ model were JRPRC module for clear-sky photolysis rate calculation, initial condition (ICON) module for initial chemical conditions, boundary condition (BCON) module for dynamic boundary conditions of the modeling domain, and CCTM module for continuous atmospheric chemical simulation. The specific CMAQ information can be obtained from Ou et al. (2016). Simulation was conducted for the entire month of September 2017 with significant O_3 pollution. The first three-day simulation was treated as spin-up time and the model outputs were not included in the analysis.

The hourly observations on atmospheric temperature, wind speed and O_3 concentration at seven sites across the PRD, including Jiangmen, Foshan, Guangzhou, Zhuhai, Shenzhen, Zhongshan, and Huizhou, were used to evaluate model performance on replicating meteorological variables and ambient O_3 level. **Fig. S1b** shows the geographical locations of the seven sites. Correlation coefficient (R) and mean bias (MB) between observed and simulated values were calculated, as shown in **Tables S4** and **S5**.

1.2. *Identification of O_3 formation regime*

As shown in **Fig. S2**, an emission reduction matrix, including 1 base case and 39 emission reduction scenarios with AVOCs and NO_x emission reductions in various degrees (% change in gram), was designed to examine O_3 changes in response of AVOCs and NO_x reductions (Kinosian, 1982; Ou et al., 2016). Emission reductions were only conducted for D3, and only AVOCs were considered as BVOCs emissions are uncontrollable. O_3 isopleth diagrams were plotted by interpolating O_3 concentrations at different AVOCs and NO_x reductions and were used to identify O_3 formation regime on each day in September 2017.

In order to quantitatively identify O_3 formation regime, we calculated T which is the ratio between O_3 change in response to 10% reduction of NO_x emission and that in response to 10% reduction of AVOCs emission. A T value less than 0.5 indicates AVOCs-limited O_3 formation regime, 0.5 to 2 for a transitional regime, and higher than 2 for a NO_x-limited regime (Sillman and West, 2009; Li et al., 2018).

1.3. *Process analysis*

We applied PA to estimate contributions to a particular species from different physical and chemical processes at each integration time step over each grid (Zhao et al., 2019). The WRF-CMAQ model calculates the time rates of change in chemical species concentrations (c_i) by using the following mass continuity equation,

$$\frac{\partial C_i}{\partial x} = -\left(u\frac{\partial C_i}{\partial x} + v\frac{\partial C_i}{\partial y}\right) - w\frac{\partial C_i}{\partial z} + \frac{\partial}{\partial z}\left(K_e\frac{\partial C_i}{\partial z}\right) + \left(\frac{\partial C_i}{\partial t}\right)_{cloud} + R + D + E \quad (1)$$

u, v, and w denote the components of wind speed in the three directions, respectively, and K_e is turbulent diffusivity. The seven terms on the right-hand side in Eq. (1) represent horizontal advection, vertical advection, vertical diffusion, cloud processes, chemical reactions (R), dry deposition (D), and source emission rate (E), respectively. PA was per-

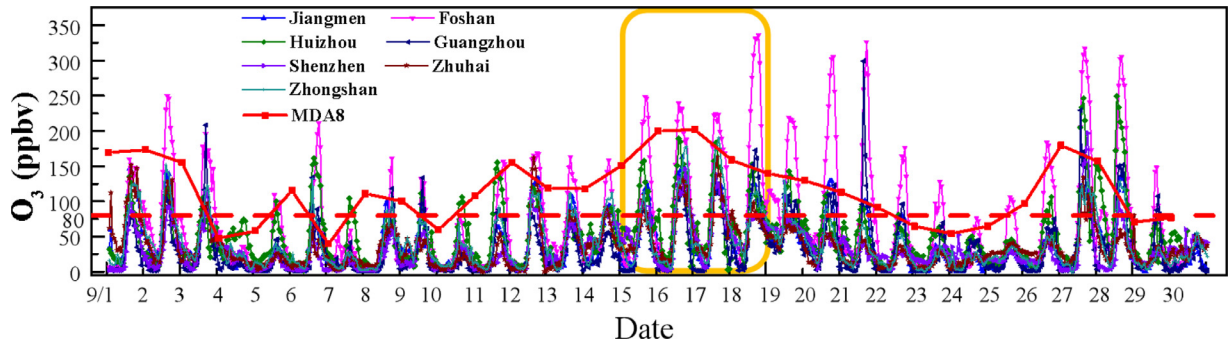

Fig. 1 – Time series of observed hourly O_3 concentration (thin line) and averaged 8-h maximum O_3 concentration (red thick line) in September 2017. The O_3 episode during 15-19 is highlighted in a yellow box. (red dashed line: the national tier-II standard of 80 ppbv).

formed over D3 at 11:00–16:00 every day when O_3 peaks occurred Liu and Roy (2015).

1.4. *Indicator evaluation metrics*

In this section, we developed a method to evaluate the performance of indicators in distinguishing O_3 formation regime. By identifying the O_3 formation regime and indicator values on each day of September 2017, we may calculate the value ranges of all indicators under the three O_3 formation regimes in the entire month. The performance of indicators was evaluated by two factors, the percentage of overlap between the three regimes and the number of the days in the overlap. The percentage of overlap, P, for a specific indicator was quantified using the following equation:

$$P = \frac{O_{max} - O_{min}}{T_{max} - T_{min}} \quad (2)$$

where, O_{max} and O_{min} represent the maximum and minimum value of the overlap range, and T_{max} and T_{min} denote the maximum and minimum value of the indicator, respectively. The smaller the percentage of overlap and the number of days in the overlap are, the better the indicator in distinguishing O_3 formation regimes.

2. Results and discussion

2.1. *General characteristics of O_3 episode in September 2017*

Fig. 1 depicts the hourly averaged O_3 concentrations at the seven sites over the PRD during September 2017. There were 21 days with MDA8 O_3 concentration over the national tier-II standard of 160 μg/m^3 (~80 ppbv), indicating a continuous and long-lasting O_3 elevation event. The most significant O_3 episode occurred during 15–19, with the MDA8 O_3 exceeding 200 ppbv at some stations. The highest hourly O_3 concentration of 336 ppbv was recorded at Foshan on 18. This O_3 episode was associated with three synoptic patterns, i.e., approaching of a tropical cyclone on 15–16, eastward movement of a high pressure ridge on 17, and extension of Western Pacific Subtropical High (WPSH) on 18–19, as shown in the weather maps of **Fig. S3** (Jian et al., 1998; Shen et al., 2015). On 15-16 when a tropical cyclone was located 500-800km to the PRD, PRD was controlled by the subsidence air in the outskirt of the tropical cyclone, leading to strong solar radiation, high temperature and a stabilized atmospheric structure. The background winds were weak and the dispersion capacity was largely hindered, favoring local pollutant accumulation and photochemical reaction. On 17 when PRD was located in front of a ridge, the coupling between upper-level convergence and low-level divergence led to vertical downward movement, which favored transport of O_3 from upper level. On 18-19, PRD was gradually controlled by the westward extension of WPSH. Located between WPSH and a low pressure system over Gulf of Tonkin, PRD was prevailed by easterly wind due to pressure gradient, favoring horizontal O_3 transport.

We conducted meteorology and O_3 simulations for the entire September. In terms of meteorology, better model performance in temperature than wind speed simulation was discovered, as shown in **Table S4**. Relatively poorer simulation of wind speed was largely due to the kind of outdated land use information which cannot well capture land use changes in the rapid urbanization process in the past decade. A comparison between O_3 observations and simulation is presented in **Fig. S4**, and the statistics is provided in **Table S5**. Overall, the model had a good performance in O_3 simulation, with correlation coefficient (R) of 0.71 and mean bias (MB) of 4.7, which were well above the recommended values by US EPA (Emery et al., 2017). The model was able to capture diurnal variation of O_3 at different sites, but underestimated O_3 peak levels during O_3 episode and overestimated O_3 levels at night. The under-prediction of O_3 peaks during daytime is mainly related to the uncertainties of emissions and over-predicted wind speed (Zhao et al., 2019). The nighttime over-predictions of surface O_3 might be collectively caused by inaccuracies in nighttime NO_3 chemistry Dimitroulopoulou and Marsh (1997) and meteorological inputs such as boundary layer height and vertical motion (Zhao et al., 2019), as well as uncertainties in emissions of O_3 precursors.

2.2. *Atmospheric oxidation during O_3 episode*

As explained in Section 1, HO_x radicals play a critical role in atmospheric oxidation and O_3 production. In this section, we in-

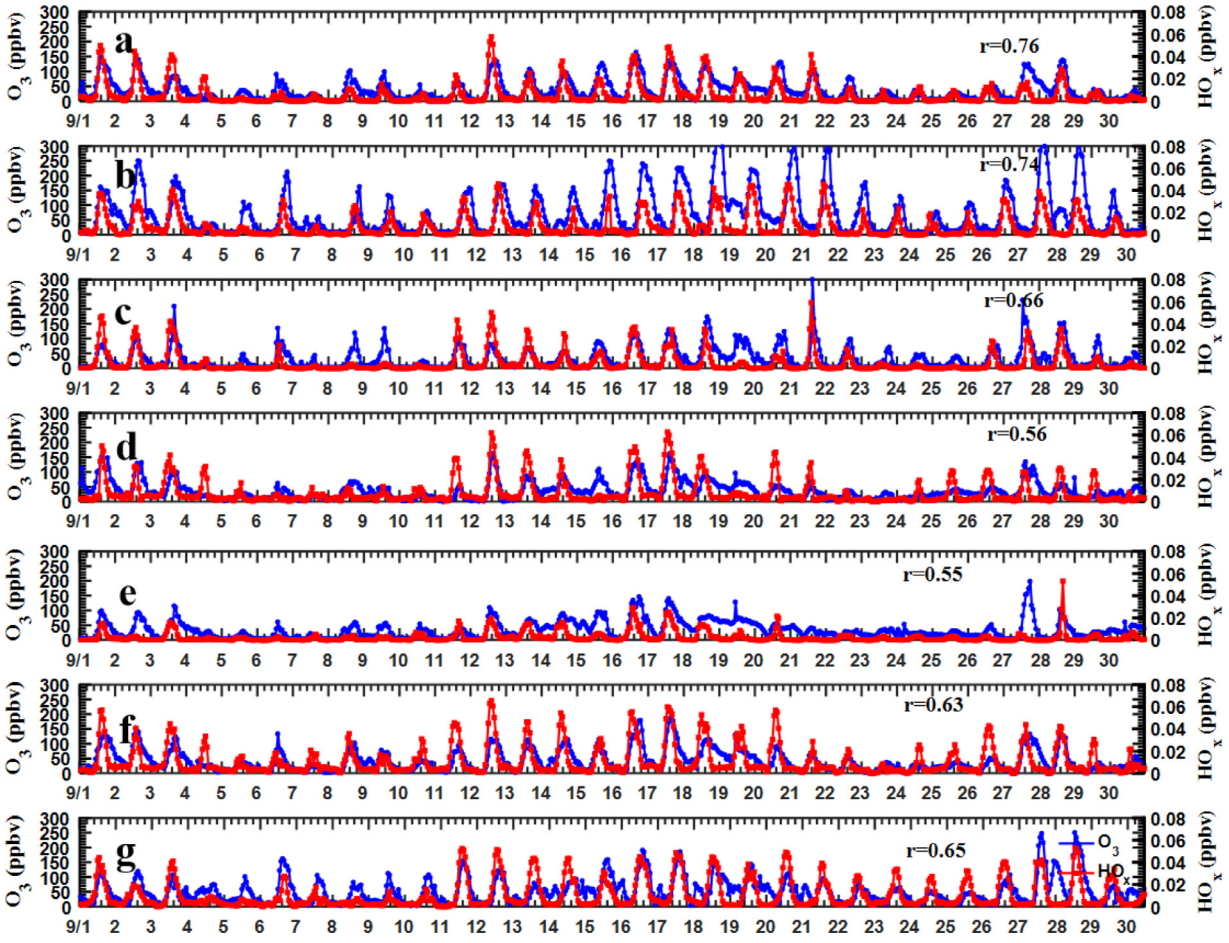

Fig. 2 – Time series of simulated HO_x (red) and observed O_3 (blue) concentrations at (a) Jiangmen, (b) Foshan, (c) Guangzhou, (d) Zhuhai, (e) Shenzhen, (f) Zhongshan, and (g) Huizhou during September 2017.

vestigated the relationship between HO_x radicals and O_3 budget.

Fig. 2 compares simulated HO_x with observed O_3 concentrations during the entire month of September 2017. The simulated daily peak OH and HO_2 values were in the range of 0.15-0.65 pptv and 21-65 pptv, respectively, during the entire month of September 2017. Due much to the fact that the OH and HO_2 observational data is very scarce, we further compare the CMAQ-simulated concentrations of HO_x radicals with a set of earlier studies (Hofzumahaus, et al., 2009; Mao et al., 2010; Ren et al., 2013), as shown in **Fig. S5**. A similar diurnal variation with same magnitude of HO_x radicals was found. The results indicate that the model was comparable to those published. These values were higher than those in the other regions worldwide, such as 0.6 pptv for OH and 40 pptv for HO_2 in Houston and 0.35 pptv for OH and 10 pptv for HO_2 in New York City (Ren et al., 2013; Mao et al., 2010), and were comparable with those observed over the PRD in the summer of 2006 (Hofzumahaus et al., 2009). Diurnally, both OH and HO_2 had maxima in the afternoon with peaking time around 14:00-16:00 and minima at night. Day-to-day co-variations between HO_x and O_3 concentrations can be also noticed. Correlation coefficients were higher than 0.55 at all sites.

Similar spatial distributions of HO_x and O_3 concentrations was also revealed, as shown in **Fig. S6** using the 15-19 episode as an example. A HO_x and O_3 concentration hotspot was noted over central PRD, which further indicated that HO_x radicals play a critical role in O_3 production. In addition, a clear relationship between large-scale circulation and accumulation and transport of O_3 was noticed. On 15-16, typhoon Taili in the South China Sea brought about stabilized atmospheric structure, weak surface winds, strong solar radiation and high temperature over the PRD, which were conducive to the formation and accumulation of O_3. Afterwards, a northward movement of O_3 and HO_x hotspot areas from central PRD were noticed, which corresponded to the eastward movement of a strengthened ridge on 17 and extension of WPSH on 18-19. Thus, the strengthened O_3 and HO_x episode over the PRD were mainly driven by the variation of large-scale circulation.

2.3. *Impact of atmospheric oxidation on O_3 formation regimes*

In the previous section, we discovered a clear connection between atmospheric oxidation and O_3 production over the PRD. The O_3 production rate is essentially driven by the production

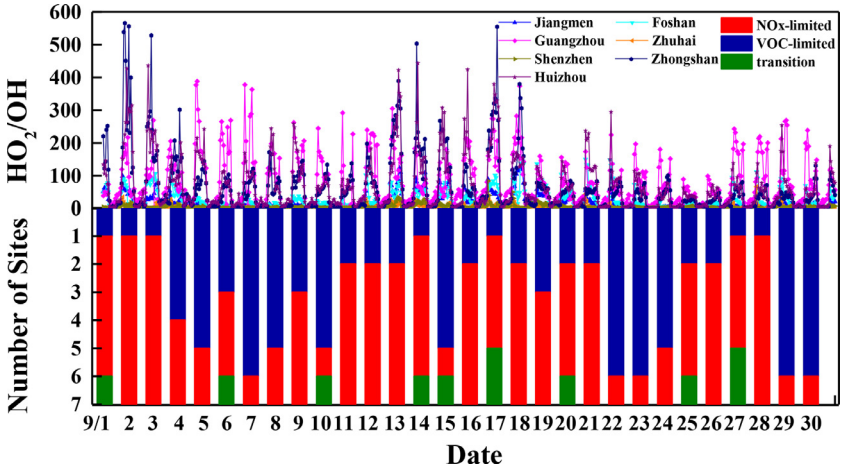

Fig. 3 – Time series of HO_2/OH ratio at each site (curve) and number of sites in three O_3 formation regimes (bar) during September 2017. Bars in red, green and blue represent NO_x-limited, transitional, and VOC-limited regime, respectively.

rate of NO_2 which is closely associated with two main reactions (HO_2 + NO and RO_2 + NO). When O_3 formation is in the VOC-limited regime, higher amount of HO_x favors transformation from NO to NO_2, accelerating NO_x cycle and leading to O_3 formation. Abundant NO is ready to convert HO_2 to OH, lowering HO_2/OH ratio. In the NO_x-limited regime, OH reacts with VOCs to produce organic peroxy radicals (RO_2). RO_2 oxidizes NO to produce NO_2, and the photolysis of NO_2 produces O atom and further reacts with O_2 to form O_3. Excessive HO_2 radical is generated by the RO+O_2 and OH+VOCs reactions, elevating HO_2/OH ratio. Thus, we expect that the HO_2/OH ratio have a close relationship with O_3 formation regime, which is examined in this section.

By doing a set of sensitivity study described in Section 2.2, we developed O_3 isopleth diagram to identify O_3 formation regime at different sites over the PRD. The shapes of O_3 isopleths varied greatly on the different days, indicating varied O_3 formation regimes under the base condition. For example, at Zhuhai site during the 15-19 episode, O_3 formation regime fluctuated between VOC-limited, and NO_x-limited regimes, as illustrated in **Fig. S7**. This highlighted significant variation in O_3 formation mechanisms over the PRD, even within a single O_3 pollution event.

We further examined the co-variations of HO_2/OH and O_3 formation regime during the entire month of September. A clear correspondence was found, as shown in Fig. 3. As expected, HO_2/OH was higher when O_3 formation regime shifted to NO_x-limited and lower when O_3 formation regime shifted to VOC-limited. However, there was a spatial heterogeneity of HO_2/OH threshold ratios for O_3 formation regime differentiation, as indicated in Table 1. The cities were generally split into two clusters, with Huizhou, Zhongshan, Shenzhen and Zhuhai having HO_2/OH threshold values around 9–12 and Guangzhou, Jiangmen and Foshan around 5–6. The mis-matching ratios of VOC- and NO_x-limited regimes inferred from HO_2/OH ratios and scenario analysis were less than 16%, indicating HO_2/OH is a good indicator for O_3 formation regime. The mis-matching ratios of transitional regime were a bit higher due much to the limited number of days falling within this regime.

Table 1 – Distribution of HO_2/OH values for different O_3 formation regime and the percentages of mis-matches during the entire month

Site	NO_x-limited	Transitional	VOC-limited
Jiangmen	>5.5 (12%)	5-5.5 (0%)	<5 (9%)
Foshan	>5.2 (5%)	4.2-5.2 (50%)	<4.2 (0%)
Guangzhou	>2.5 (0%)	2-2.5 (50%)	<2 (16%)
Zhuhai	>10 (14%)	9.5-10 (25%)	<9.5 (8%)
Shenzhen	>10 (0%)	9.7-10 (0%)	<9.7 (0%)
Zhongshan	>10.8 (8%)	9.9-10.8 (0%)	<9.9 (0%)
Huizhou	>12 (0%)	10-12 (0%)	<10 (0%)

To better identify the underlying reason for the spatial heterogeneity of HO_2/OH threshold ratios for O_3 formation regime, we further investigated the spatial distribution of NO_x and VOC emissions over the PRD, as shown in **Fig. S8**. We noticed that these three sites (ie. Jiangmen, Foshan, and Guangzhou) located at red hotspot area with the NO_x emission intensity of 0.20, 0.32, and 0.25 mole/sec, respectively (**Table S6**). For the other four sites, relatively lower NO_x emission intensity was found (0.08 mole/sec for Zhuhai, 0.10 mole/sec for Shenzhen, 0.11 mole/sec for Zhongshan, and 0.03 mole/sec Huizhou). Previous studies have demonstrated that the model always underestimated HO_2 at high NO levels in most ground-based campaigns, which may cause a lower HO_2/OH ratio over central and western PRD (Martinez et al., 2003; Ren et al., 2006). Ren et al., (2003) also noticed a similar under-predicted HO_2 under high NO concentration with NCAR chemical ionization mass spectrometer (CIMS). Their results further proved that the uncertainties in the model at high NO_x is responsible for the under-predicted HO_2.

We further compared O_3 formation regimes estimated by both HO_2/OH ranges listed in Table 1 and scenario analysis during the 15–19 episode, as shown in Fig. 4. Good consistency in O3 formation regimes were discovered. This highlighted the powerfulness of using HO_2/OH to indicate O_3 formation

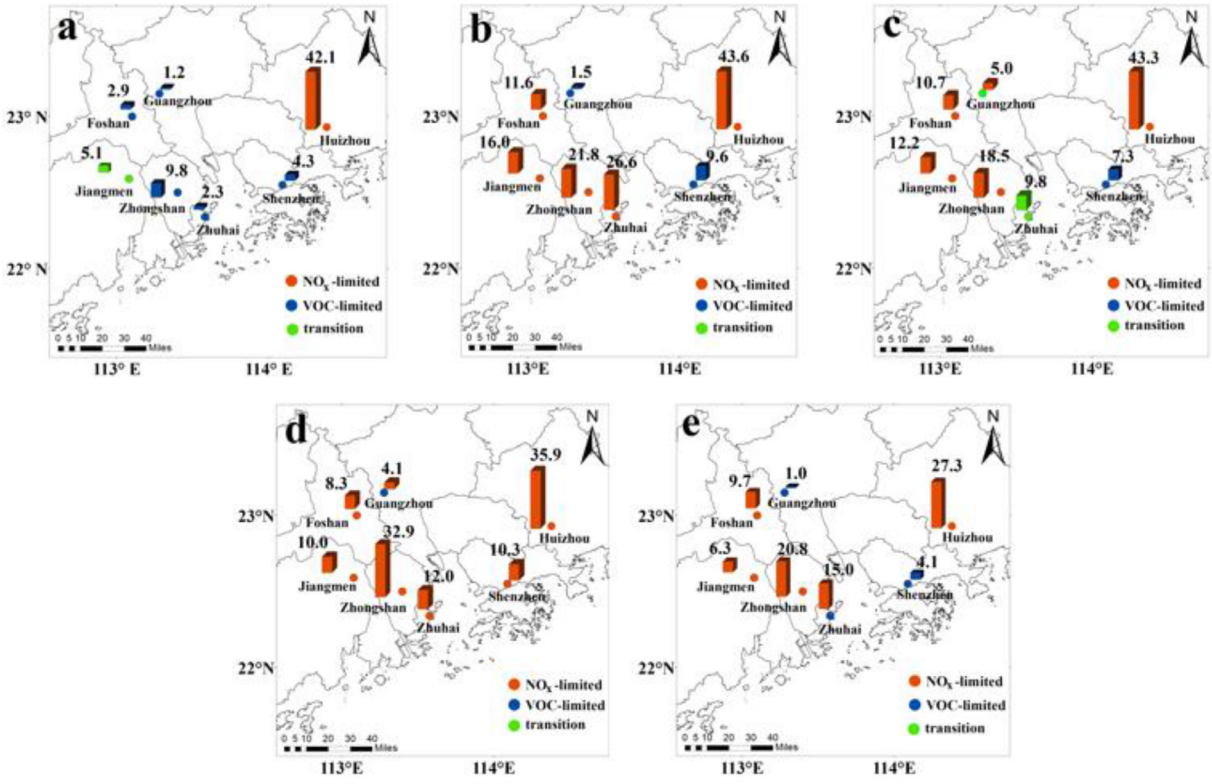

Fig. 4 – Spatial distribution of O_3 formation regime and HO_2/OH ratio at 7 sites on (a) 15, (b) 16, (c) 17, (d) 18 and (e) 19 September. Bars in red, green and blue represent NO_x-limited, transitional, and VOC-limited regime, respectively, based on the HO_2/OH ranges listed in Table 1. Numbers above the bars are the corresponding HO_2/OH ratios. Points in red, green and blue represent NO_x-limited, transitional, and VOC-limited regime identified by sensitivity analysis, respectively.

regime, even in the context of drastically changing O_3 formation mechanisms as a result of a wide span of large-scale circulation patterns occurred during this episode. Only exceptions were revealed at Guangzhou on 17 and 18 and Zhuhai on 19 when HO_2/OH and scenario analysis inferred different O_3 formation regimes. HO_2/OH indicator suggested NO_x-limited regime for all three cases while scenario analysis estimated transitional on 17 at Guangzhou and VOC-limited on 18 at Guangzhou and 19 at Zhuhai. We will examine the underlying reason for such discrepancies in the following section.

2.4. *Identification of underlying reasons of the relationship between O_3 formation and atmospheric oxidation*

To better identify the underlying factors for the relationship between HO_2/OH and O_3 formation regime, we performed PA to retrieve physical and chemical contributions to O_3 increase during the 15-19 episode, as listed in Table 2. The PA results listed in Table 2 represent a domain average. Chemical processes contributed predominantly to O_3 increase on all days, as a result of favorable meteorological conditions. Physical processes, including horizontal transport and vertical advection, posed substantially less or even negative contributions to O_3 increase.

We further investigated physical and chemical contributions to O_3 changes at each site during this episode, as shown in Fig. 5. The PA results presented in Fig. 5 represent a closest grid to each site. We noticed that overall, chemical reaction contributed predominantly to O_3 changes. Exceptional cases with higher physical than chemical contributions, i.e. Guangzhou on 17 and 18 and Zhuhai on 19, are highlighted by yellow boxes. Interestingly, these three cases coincided exactly with those having discrepancies in O_3 formation regimes inferred by HO_2/OH and scenario analysis. This likely indicated a causal relationship between greater physical contribution and discrepancies in O_3 formation regimes. Extending this analysis to the entire September, we found that about 95% (18 out of 19) of discrepancy cases were associated with larger physical than chemical contributions, which gave further weight to the causal relationship. As an indicator essentially delineating atmospheric oxidation capacity, HO_2/OH is

Table 2 – Contribution of physical and chemical processes to O_3 increase during 15-19 September

Date	Physical process (ppbv/hr)	Chemical process (ppbv/hr)	Net (ppbv/hr)
15 Sep	1.0	5.9	6.9
16 Sep	-0.5	8.3	7.8
17 Sep	-1.5	8.7	7.2
18 Sep	-0.2	6.1	5.9
19 Sep	0.7	4.2	4.9

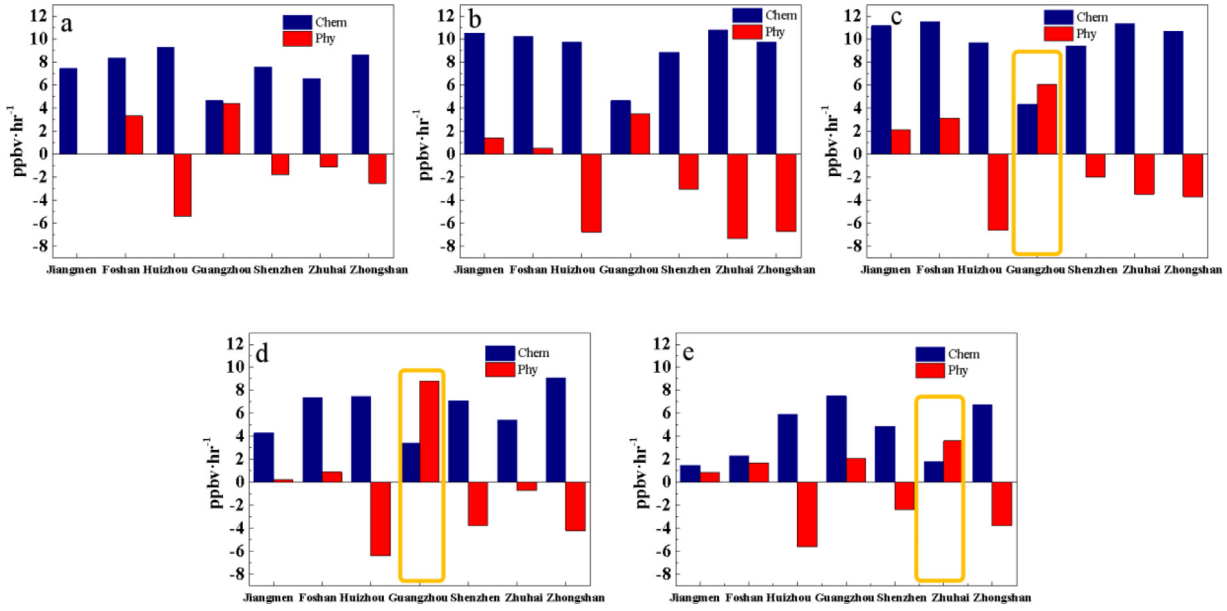

Fig. 5 – Physical and chemical contributions to O_3 changes on (a) 15, (b) 16, (c) 17, (d) 18, and (e) 19 September at the seven sites across the Pearl River Delta retrieved by process analysis. Cases with discrepancies in O_3 formation regimes inferred by HO_2/OH and scenario analysis are highlighted in yellow boxes.

Table 3 – Percentage of overlap and number of the days in the overlap for all indicators at the seven sites across the Pearl River Delta

Site	HO_2/OH	H_2O_2/HNO_3	H_2O_2/NO_y	H_2O_2/NO_z	O_3/HNO_3	O_3/NO_y	O_3/NO_z
Jiangmen	2.7% (5)	49.9% (28)	36.3% (23)	48.9% (25)	66.9% (29)	98.6% (28)	37.5% (21)
Foshan	0.3% (2)	24.5% (29)	30.3% (19)	55.0% (25)	46.6% (28)	100% (30)	87.6% (26)
Guangzhou	56.3% (13)	100% (30)	88.6% (26)	100% (30)	99.2% (29)	97.1% (29)	49.1% (24)
Zhuhai	34.8% (20)	100% (30)	100% (30)	65.6% (29)	38.2% (28)	89.3% (27)	47.7% (26)
Shenzhen	0% (0)	93.7% (23)	60.9% (12)	94.9% (25)	85.5% (18)	60.5% (8)	86.4% (20)
Zhongshan	10.4% (5)	15.9% (23)	64.3% (25)	52.4% (25)	4.0% (15)	100% (30)	10.5% (15)
Huizhou	0% (0)	65.7% (28)	24.5% (11)	7.5% (11)	43.0% (29)	99.3% (29)	6.7% (6)

theoretically associated with O_3 that is produced by chemical reactions. Substantial transport of O_3 would change the O_3-precursor nonlinearity, thereby negating the linkage between HO_2/OH and O_3 formation regime. As only 9% (19 out of 210) of cases with higher physical than chemical contributions in the entire month, we still believe HO_2/OH is a good indicator in signaling O_3 formation regime over the PRD. Our results also underscored the necessity in conducting more simulations to quantify the threshold of HO_2/OH indicator at sites where physical process had greater contribution to O_3 changes.

Physical processes, including horizontal transport and vertical advection, contribute to O_3 changes and impact O_3 formation regime at a particular area. To better identify the proportion of the contribution of horizontal transport and vertical transport varies under different synoptic circulation types, we further calculated contributions of horizontal transport and vertical transport in the mis-matching cases. On 17 at Guangzhou, the contributions of horizontal and vertical transport to surface O_3 were -12 and 18.1 ppbv/hr, respectively. Significant contribution from vertical transport was caused by subsidence of air from the upper-layer. Conversely, horizontal transport played a positive role to O_3 with average contributions of 19 ppbv/hr on 18 at Guangzhou and 13 ppbv/hr on 19 at Zhuhai, while vertical transport was negative. Contribution of horizontal transport indicated that a large amount of O_3 from the upwind area were transported to Guangzhou and Zhuhai through easterly winds. Our analysis revealed that horizontal and vertical transport contributed differently in the mismatching cases under different large-scale circulation types, which indicated that the large-scale circulation played an important role in shaping O_3 formation regime over the PRD.

Since a few uncertainties remain in HO_2/OH indicator, a long-period simulation together with more observations are needed to quantify the threshold of HO_2/OH indicator in different sites. Besides, the results also indicate the great importance of promoting measurement of atmospheric radicals to gain insight in atmospheric processes leading to O_3 pollution.

2.5. *Comparison between HO_2/OH and other indicators in indicating O_3 formation regime*

In this section, we compared the performance of a series of photochemical indicators with a same criterion at each site, including HO_2/OH, H_2O_2/HNO_3, H_2O_2/NO_y, H_2O_2/NO_z,

O_3/HNO_3, O_3/NO_y and O_3/NO_z, in indicating O_3 formation regimes. First, we developed O_3 isopleth diagram to identify O_3 formation regime at different sites over the PRD as described in Section 2.2. Second, we investigate the distribution of the ratio of each indicator under the three O_3 formation regimes. And finally, as described in Section 2.4, the percentage of overlap and the number of the days in the overlap were used to evaluate the performance, as listed in Table 3.

It is noted that at Jiangmen, Foshan, Zhuhai, Shenzhen and Huizhou, HO_2/OH showed the best performance with the lowest percentage of overlap and the number of the days in the overlap. In particular, there was no overlap at Shenzhen and Huizhou, meaning HO_2/OH can indicate O_3 formation regimes with 100% accuracy. At Guangzhou and Zhongshan, although the percentage of overlap of HO_2/OH was the second lowest (56.3% for HO_2/OH vs. 49.1% for O_3/NO_z at Guangzhou and 10.4% for HO_2/OH vs. 4.0% for O_3/HNO_3 at Zhongshan), the number of days was the lowest and much smaller than the second lowest value (13 for HO_2/OH vs. 24 for O_3/NO_z at Guangzhou and 5 for HO_2/OH vs. 15 for O_3/HNO_3 and O_3/NO_z at Zhongshan).

Therefore, we believe HO_2/OH is the best indicator to distinguish O_3 formation regimes over the PRD. This also highlights the fact that atmospheric oxidation is the core driver of O_3 formation regimes in a photochemically active region. Using HO_2/OH to identify O_3 formation regimes circumvents the time-consuming sensitivity analysis by numerical models which very often involves tens of scenarios, thereby providing a simple and direct way for fast identification of O_3 formation regimes which is essential to formulate contingency control strategies to mitigate O_3 pollution during episode.

3. Conclusions

PRD has been suffering from significant and worsening O_3 pollution which is largely driven by the high oxidative capacity over the region. A set of studies have been performed to investigate the impact of the atmospheric oxidation on O_3 production, but the impacts of atmospheric oxidation on O_3-precursor nonlinearity and O_3 formation regimes, the essential indicators for O_3 pollution control, still remain a large knowledge gap. In this study, a comprehensive air quality model (WRF-CMAQ) was used to investigate the relationship between atmospheric oxidation and O_3 formation regimes during the entire month of September 2017 with 21 days with MDA8 O_3 concentration over the national tier-II standard.

A detailed investigation of the mechanism of atmospheric oxidation, especially the role of HO_x radicals in shaping O_3 formation regimes is required over the PRD. We discovered a clear relationship between oxidative capacity and O_3 formation regime over the PRD. The O_3 formation is dominated by NO_x-limited regime when the HO_2/OH ratio is approximately higher than 11 and lower than 9.5 when dominated by VOC-limited over eastern PRD. Over central and western PRD, an HO_2/OH ratio higher than 5 and lower than 2 was indicative of NO_x-limited and VOC-limited regime, respectively.

PA results denote that the HO_2/OH indicator exhibits a good performance on O_3 formation judgment when the chemical reaction contributed predominantly to O_3 changes. Physical contribution, including horizontal transport and vertical transport, may pose uncertainties on the indication of O_3 formation regime by HO_2/OH ratio. Substantial transport of O_3 would change the O_3-precursor nonlinearity, thereby negating the relationship between HO_2/OH and O_3 formation regime. As only 9% of cases with higher physical than chemical contributions in the entire month, we believe HO_2/OH is a good indicator in signaling O_3 formation regime over the PRD. In comparison with other commonly used photochemical indicators, the HO_2/OH indicator showed a lower range of the percentage of overlap and the limited number of the days in the overlap at each site. Thus, HO_2/OH ratio had the best performance in differentiating NO_x-, transition, and VOC-limited regimes.

Due much to the fact that the observational data of HO_2 and OH is very scarce, we would currently recommend using the model simulation to obtain the HO_2/OH ratio. Although there are some uncertainties in simulation results, it is a simple and direct way for fast identification of O_3 formation regimes.

This study has an important implication on understanding the relationship between atmospheric oxidation and O_3 formation regimes during O_3 episodes. Using HO_2/OH to identify O_3 formation regimes circumvents the time-consuming sensitivity analysis by numerical models, thereby providing a simple and direct way for fast identification of O_3 formation regimes which is essential to formulate contingency control strategies to mitigate O_3 pollution during episode. The results also underscored the importance of characterizing behaviors of radicals to gain insight in atmospheric processes leading to O_3 and other secondary pollution over a photochemically active region.

Acknowledgement

This work is sponsored by the National Natural Science Foundation of China (Nos. 91644221, 41575009).

Appendix A. Supplementary data

Supplementary material associated with this article can be found, in the online version, at doi:10.1016/j.jes.2020.09.038.

REFERENCES

Ainsworth, E.A., Yendrek, C.R., Sitch, S., Collins, W.J., Emberson, L.D., 2012. The effects of tropospheric ozone on net primary productivity and implications for climate change. Annu. Rev. Plant. Biol. 63, 637–661.

Cardelino, C.A., Chameides, W.L., 1995. An observation-based model for analyzing ozone precursor relationships in the urban atmosphere. J. Air. Waste. Manag. Assoc. 45, 161–180. doi:10.1080/10473289.1995.10467356.

Chan, C.K., Yao, X., 2008. Air pollution in mega cities in China. Atmos. Environ. 42, 1–42. doi:10.1016/j.atmosenv.2007.09.003.

Cheng, H., Guo, H., Wang, X., Saunders, S.M., Lam, S.H.M., Jiang, F., et al., 2010. Erratum to: on the relationship between ozone and its precursors in the pearl river delta: application of an observation-based model (OBM). Environ. Sci. Pollut. R. 17, 1491–1492. doi:10.1007/s11356-010-0347-6.

Dimitroulopoulou, C., Marsh, A.R.W., 1997. Modelling studies of NO_3 nighttime chemistry and its effects on subsequent ozone formation. Atmo. Environ. 31, 3041–3057.

Emery, C., Liu, Z., Russell, A.G., Odman, M.T., Yarwood, G., Kumar, N., 2017. Recommendations on statistics and benchmarks to assess photochemical model performance. J. Air. Waste. Manage. 67, 582–598. doi:10.1080/10962247.2016.1265027.

Guenther, A., Jiang, J., Heald, C., Sakulyanontvittaya, Duhl.T., Emmons, L., Wang, J., 2012. The model of emissions of gases and aerosols from nature version 2.1 (MEGAN2.1): an extended and updated framework for modeling biogenic emissions. Geosci. Model Dev. 6, 1471–1492. doi:10.5194/gmd-5-1471-2012.

Hofzumahaus, A., Rohrer, F., Lu, K., Bohn, B., Brauers, T., Chang, C.C., et al., 2009. Amplified trace gas removal in the troposphere. Science 324, 1702–1704.

Huang, X., Ding, A., Gao, J., Zheng, B., Zhou, D., Qi, X., et al., 2020. Enhanced secondary pollution offset reduction of primary emissions during COVID-19 lockdown in China. Natl. Sci. Rev. nwaa 137. https://doi.org/10.1093/nsr/nwaa137.

Jaeglé, L., Jacob, D.J., Brune, W.H., Tan, D., Faloona, I.C., Weinheimer, A.J., et al., 1998. Sources of HOx and production of ozone in the upper troposphere over the United States. Geophys. Res. Lett. 25, 1709–1712.

Jian, Z., Rao, S.T., Daggupaty, S.M., 1998. Meteorological Processes and Ozone Exceedances in the Northeastern United States during the 12-16 July 1995 Episode. J. Appl. Meteorol 37, 776–789.

Jiménez, P., Baldasano, J.M., 2004. Ozone response to precursor controls in very complex terrains: use of photochemical indicators to assess O_3-NO_x-VOC sensitivity in the northeastern Iberian Peninsula. J. Geophys. Res. 109. https://doi.org/10.1029/2004JD004985.

Kinosian, R.J., 1982. Ozone-precursor relationships from EKMA diagrams. Environ. Sci. Technol. 16, 880–883.

Kleinman, L.I., Daum, P.H., Lee, J.H., Lee, Y.N., Nunnermacker, L.J., Springston, S.R., et al., 1997. Dependence of ozone production on NO and hydrocarbons in the troposphere. Geophys. Res. Lett. 24, 2299–2302. doi:10.1029/97GL02279.

Kumar, N., Russell, A.G., 1996. Comparing prognostic and diagnostic meteorological fields and their impacts on photochemical air quality modeling. Atmos. Environ. 30, 1989–2010. https://doi.org/10.1016/1352-2310(95)00179-4.

Kurokawa, J., Ohara, T., Morikawa, T., Hanayama, S., Greet, J.M., Fukui, T., et al., 2013. Emissions of air pollutants and greenhouse gases over Asian regions during 2000-2008: regional emission inventory in Asia (REAS) version 2. Atmos. Chem. Phys. 13, 10049–10123. doi:10.5194/acpd-13-10049-2013.

Le, T., Wang, Y., Liu, L., Yang, J., Yung, Y.L., Li, G., et al., 2020. Unexpected air pollution with marked emission reductions during the COVID-19 outbreak in China. Science doi:10.1126/science.abb7431.

Li, Q., Zhang, L., Wang, T., Wang, Z., Fu, X., Zhang, Q., 2018. "New" reactive nitrogen chemistry reshapes the relationship of ozone to its precursors. Environ. Sci. Technol. 52, 2810–2818.

Li, Y., Lau, A.K.H., Fung, J.C.H., Zheng, J., Liu, S., 2013. Importance of NO_x control for peak ozone reduction in the pearl river delta region. J. Geophys. Res. Atmos. 118, 9428–9443. doi:10.1002/jgrd.50659.

Liu, X., Zhang, Y., Xing, J., Zhang, Q., Wang, K., Streets, D.G., et al., 2010. Understanding of regional air pollution over China using CMAQ, part II. Process analysis and sensitivity of ozone and particulate matter to precursor emissions.. Atmos. Environ. 44, 3719–3727. https://doi.org/10.1016/j.atmosenv.2010.03.036.

Liu, Z., Roy, S.S., 2015. Spatial patterns of seasonal level diurnal variations of ozone and respirable suspended particulates in Hong Kong. Prof. Geogr. 67, 17–27.

Logan, J.A., 1989. Ozone in rural areas of the United States. J. Geophys. Res. Atmos. 94, 8511–8532.

Lu, H., Lyu, X., Cheng, H., Ling, Z., Guo, H., 2019. Overview on the spatial-temporal characteristics of ozone formation regime in China. Environ. Sci. Proc. Impacts doi:10.1039/C9EM00098D.

Mao, J., Ren, X., Chen, S., Brune, W.H., Chen, Z., Martinez, M., et al., 2010. Atmospheric oxidation capacity in the summer of Houston 2006: comparison with summer measurements in other metropolitan studies. Atmos. Environ. 44, 4107–4115.

Martinez, M., Harder, H., Kovacs, T.A., Simpas, J.B., Bassis, J., Lesher, R., et al., 2003. OH and HO_2 concentrations, sources, and loss rates during the Southern Oxidants Study in Nashville, Tennessee, summer 1999. J. Geophys. Res. Atmos 108, 17.

Monks, P.S., 2005. Gas-phase radical chemistry in the troposphere. Chem. Soc. Rev. 34, 376–395.

Ou, J., Yuan, Z., Zheng, J., Huang, Z., Shao, M., Li, Z., et al., 2016. Ambient ozone control in a photochemically active region: short-term despiking or long-term attainment? Environ. Sci. Technol. 6b-345b.

Ren, X.R., Brune, W.H., Mao, J.Q., Mitchell, M.J., Lesher, R.L., Simpas, J.B., et al., 2006. Behavior of OH and HO_2 in the winter atmosphere in New York City. Atmos. Environ. 40, S252–S263.

Ren, X.R., Edwards, G.D., Cantrell, C.A., Lesher, R.L., Metcalf, A.R., Shirley, T., et al., 2003. Intercomparison of peroxy radical measurements at a rural site using laser-induced fluorescence and peroxy radical chemical ionization mass spectrometer (PerCIMS) techniques. J. Geophy. Res. Atmos. 108, 9.

Ren, X., van Duin, D., Cazorla, M., Chen, S., Mao, J., Zhang, L., et al., 2013. Atmospheric oxidation chemistry and ozone production: results from SHARP 2009 in Houston, Texas. J. Geophys. Res. Atmos. 118, 5770–5780. doi:10.1002/jgrd.50342.

Shao, M., Zhang, Y., Zeng, L., Tang, X., Zhang, J., Zhong, L., et al., 2009. Ground-level ozone in the pearl river delta and the roles of VOC and NOx in its production. J. Environ. Manage. 90, 512–518. https://doi.org/10.1016/j.jenvman.2007.12.008.

Sharma, S., Khare, M., 2017. Photo-chemical transport modelling of tropospheric ozone: a review. Atmos. Environ. 159, 34–54. doi:10.1016/j.atmosenv.2017.03.047.

Shen, L., Mickley, L., Tai, A., 2015. Influence of synoptic patterns on surface ozone variability over the eastern United States from 1980 to 2012. Atmos. Chem. Phys. 15. doi:10.5194/acp-15-10925-2015.

Sicard, P., De, Marco.A., Agathokleous, E., Feng, Z., Xu, X., Paoletti, E., et al., 2020. Amplified ozone pollution in cities during the COVID-19 lockdown. Sci. Total. Environ. 735, 139542.

Sillman, S., 1995. The use of NOy, H_2O_2 and HNO_3 as indicators for O_3-NOx-VOC sensitivity in urban locations. J. Geophys. Res. 100, 175–188.

Sillman, S., 1999. The relation between ozone, NOx and hydrocarbons in urban and polluted rural environments. Atmos. Environ 33, 1821–1845.

Sillman, S., He, D., 2002. Some theoretical results concerning O_3-NOx-VOC chemistry and NOx-VOC indicators. J. Geophys. Res. Atmos 107, 1–26.

Sillman, S., Logan, J.A., Wofsy, S.C., 1990. The sensitivity of ozone to nitrogen oxides and hydrocarbons in regional ozone episodes. J. Geophys. Res. Atmos. 95, 1837–1851.

Sillman, S., West, J.J., 2009. Reactive nitrogen in Mexico City and its relation to ozone-precursor sensitivity: results from photochemical models. Atmos. Chem. Phys. 9, 3477–3489.

Swackhamer, D.L., 1993. Rethinking the ozone problem in urban and regional air pollutionnational research council. national academy press (1991). J. Aerosol. Sci. 24, 977–978.

Wang, P., Chen, K., Zhu, S., Wang, P., Zhang, H., 2020. Severe air pollution events not avoided by reduced anthropogenic

activities during COVID-19 outbreak. Resour. Conserv. Recy. 158, 104814.
Wang, X., Zhang, Y., Hu, Y., Zhou, W., Zeng, L., Hu, M., et al., 2011. Decoupled direct sensitivity analysis of regional ozone pollution over the Pearl River Delta during the PRIDE-PRD2004 campaign. Atmos. Environ. 45, 4941–4949.
Westervelt, D.M., Ma, C.T., He, M.Z., Fiore, A.M., Kinney, P.L., Kioumourtzoglou, M., et al., 2019. Mid-21st century ozone air quality and health burden in China under emissions scenarios and climate change. Environ. Res. Lett. 14, 74030. doi:10.1088/1748-9326/ab260b.
Xue, L.K., Wang, T., Guo, H., Blake, D.R., Tang, J., Zhang, X.C., et al., 2013. Sources and photochemistry of volatile organic compounds in the remote atmosphere of western China: results from the Mt. Waliguan observatory.. Atmos. Chem. Phys. 13, 8551–8567.
Zhang, Y., Cooper, O.R., Gaudel, A., Thompson, A.M., Nédélec, P., Ogino, S., et al., 2016. Tropospheric ozone change from 1980 to 2010 dominated by equatorward redistribution of emissions. Nat. Geosci. 9, 875–879. doi:10.1038/ngeo2827.
Zhang, Y.H., Hu, M., Zhong, L.J., Wiedensohler, A., Liu, S.C., Andreae, M.O., et al., 2008. Regional integrated experiments on air quality over pearl river delta 2004 (PRIDE-PRD2004): overview. Atmos. Environ. 42, 6157–6173.
Zhang, Q., Streets, D.G., Carmichael, G.R., He, K.B., Huo, H., Kannari, A., et al., 2009. Asian emissions in 2006 for the NASA INTEX-B mission,. Atmos. Chem. Phys. 9, 5131–5153.
Zhao, K., Bao, Y., Huang, J., Wu, Y., Moshary, F., Arend, M., et al., 2019. A high-resolution modeling study of a heat wave-driven ozone exceedance event in New York City and surrounding regions. Atmos. Environ. 199, 368–379. https://doi.org/10.1016/j.atmosenv.2018.10.059.
Zhao, Y.B., Zhang, K., Xu, X.T., Shen, H.Z., Zhu, X., Zhang, Y.X., et al., 2020. Substantial changes in nitrogen dioxide and ozone after excluding meteorological impacts during the COVID-19 outbreak in Mainland China. Environ. Sci. Tech. Let. 7 (6), 402–408. doi:10.1021/acs.estlett.0c00304.
Zou, Y., Deng, X.J., Zhu, D., Gong, D.C., Wang, H., 2015. Characteristics of 1 year of observational data of VOCs, NOx and O3 at a suburban site in Guangzhou. China. Atmos. Chem. Phys. 15, 6625–6636.